Hot-electron production and resonance absorption of laser light in the shock-front targets

Paul Kolodner[a] and Eli Yablonovitch[b]

Gordon McKay Laboratory, Harvard University, Cambridge, Massachusetts 02138
(Received 18 August 1980; accepted 13 January 1981)

Laser targets, created by fast optical breakdown of shock fronts produced in an electrothermal shock tube filled with D_2 or H_2, have been used for studies of resonance absorption of CO_2 laser light. In these targets, the critical-surface density-gradient vector always points along the shock-tube axis, leading to reproducible hot-electron emission by plasma wave breaking. The angular distribution and energy spectrum of this emission have been studied. For 200 psec risetime laser pulses, the measured scaling of hot-electron temperature with laser pulse energy agrees with predictions of models of profile steepening by the ponderomotive force of the laser light. For 20 psec risetime laser pulses, the results are consistent with a model in which the detected electron emission is dominated by a "chirped" monoenergetic burst lasting only 1 to 2 psec. In this model, the electron energy spectrum is due to the integrated temporal variation of the enery of the burst, and the hot-electron temperature is practically independent of laser pulse energy.

I. INTRODUCTION

Resonance absorption is an extremely important mechanism by which laser light can be absorbed by hot, overdense, short-scale-length plasmas.[1] Resonance absorption is important under conditions of p-polarization and oblique incidence. It is a ubiquitous effect. Accurate tuning or phase-matching of the laser is not important for this mechanism, since a dense target will contain a critical surface for all reasonable wavelengths. The focusing conditions and original target geometry are not crucial, since the critical surface is bound to be irregular in shape; thus, there are usually regions in the plasma where the polarization and angular constraints of resonance absorption are satisfied. The magnitude of the absorption expected is sufficient to explain typical experimental observations.

A direct effect of resonance absorption is the production, via plasma "wave breaking"[2] of energetic electrons. Hot-electron "preheat" is a well-known and important threat to the success of laser fusion.

In view of the importance of these phenomena, it is surprising that there have not been more attempts at direct experimental study of resonance absorption. Its importance has been indirectly inferred from the results of second-harmonic generation experiment[3] and of calorimetric absorption experiments.[4] Hot-electron production has been indirectly studied via hard x-ray spectrum measurements.[5] The phenomenology of resonance absorption has been confirmed in microwave simulation experiments.[6] However, to our knowledge, the only direct observations of these effects in laser experiments have been our own. In a previous publication,[7] we directly observed the emission of energetic (15 keV) electrons from overdense, homogeneous gaseous targets irradiated with 500 psec CO_2 laser pulses. The emission was observed only in the plane of polarization, at oblique angles with respect to the incident laser wave vector. This was taken as direct evidence of resonance absorption. It was observed then and since, however, that the angular distribution of electron emission in these experiments is extremely unreproducible from one laser shot to the next. Since plasma wave breaking causes electron emission in a direction almost parallel to the local plasma density-gradient vector, this behavior can easily be attributed to a chaotic plasma density structure in general and an unreproducible critical-surface orientation in particular. Clearly, since resonance absorption depends strongly on the density profile in the plasma, the reprodicible study of resonant electron emission requires a target with reproducible density structure. Production of such a target has been a major goal of the work described here.

In the present experiment, the target is created by optical breakdown of a shock front in H_2 or D_2. In these gases, ionization is known[7] to occur by means of a laser-driven breakdown wave[8] which sweeps through the laser focus so quickly that the motion of ions cannot keep up with it. Thus, the density structure of the breakdown plasma is identical to that found in the un-ionized shock front. This neutral-gas shock-front density structure is an extremely reproducible function of experimentally controllable parameters. Thus, we are able to study resonance absorption in a repeatable fashion, largely in isolation from other effects.

In this work, the un-ionized shock front is created in a small, electrothermal shock tube filled with H_2 or D_2. Our short-pulse CO_2 laser system is focused onto the axis of the shock tube at an oblique angle, and, at the moment that the shock front passes into the focal region, the laser is fired. The plasma is created by optical breakdown of the shock front early in the laser pulse; this is followed by resonance absorption. We observe fast electrons emitted along the neutral-shock-front density-gradient vector; i.e., along the shock-tube axis. The experiment consists of measuring the angular distribution and energy spectrum of the electron emission. To our knowledge, these constitute the

[a] Present address: Bell Laboratories, Murray Hill, N. J. 07974.

[b] Present address: Exxon Research and Engineering, Linden, N. J. 07036.

 0031-9171/81/040759-15$00.09

only direct measurements of the properties of electron emission in resonance absorption.

In Sec. II of this paper, we briefly review some of the theory of resonance absorption, and we study the salient theoretical properties of our shock-front targets. Section III describes the experimental apparatus. In Sec. IV, the experimental results are presented. A discussion and summary follow, in Sec. V.

II. THEORY

A. Resonance absorption and electron emission

It is our intention in this section only to briefly review some well-known results from the theory of resonance absorption and related phenomena. References to detailed treatments will be given.

In resonance absorption, a p-polarized light wave is assumed to be obliquely incident on a plasma whose density n rises through the critical density n_{cr} with a scale length $n/|\nabla n| = L$. The angle of incidence, θ, is measured between the laser vacuum wave vector $\mathbf{k}_0$ and the plasma density gradient vector ∇n. In this situation, geometric optics predicts that the light wave is totally reflected from the layer where $n = n_{cr}\cos^2\theta$. From this layer, an evanescent wave can tunnel through to the critical layer; there, if the light is obliquely incident and p-polarized, the nonvanishing longitudinal component of the laser electric field can resonantly excite plasma waves.[1] In a strongly collisional plasma, the critical layer electric field is driven by this process to a value E_d/s, where $s = \nu/\omega$ is the ratio of the collision frequency ν to the laser frequency ω, and the driving field E_d is determined by the tunneling process. For a linear plasma density ramp, E_d is given by

$$E_d = [E_0/(2\pi k_0 L)^{1/2}]\phi(\tau)\,. \tag{1}$$

Here, $\tau = (k_0 L)^{1/3}\sin\theta$, E_0 is the vacuum electric field of the laser, and $\phi(\tau)$, Ginzburg's well known resonance function,[9] has the shape plotted in Fig. 1. $\phi(\tau)$ has a peak at an oblique angle of incidence θ_m given by $\tau \simeq 0.7$ or

$$3k_0 L \sin^3\theta_m \simeq 1\,. \tag{2}$$

For example, for CO_2 laser light ($\lambda = 10.6\ \mu$m) incident on a plasma with $L = 5\ \mu$m, $\theta_m \simeq 30°$.

Of course, real laser-produced plasmas are collisionless, and the resonant electric field is limited by plasma wave breaking,[2] which causes electrons to be emitted from the plasma along ∇n with energy[2]

$$\epsilon_{br} = eE_d L = eE_0(L/2\pi k_0)^{1/2}\phi(\tau)\,. \tag{3}$$

(In fact, the electric field component transverse to ∇n causes the emission to deviate slightly from this direction.) In computer simulations of resonance absorption,[2] wave breaking electrons are observed not to be monoenergetic, as predicted by Eq. (3), but rather to form a suprathermal "tail", of "temperature" $kT_h = \epsilon_{br}$, on the thermal plasma electron energy distribution. This observation yields a predicted scaling of T_h, with laser intensity I, of $T_h \propto I^{1/2}$. It is well

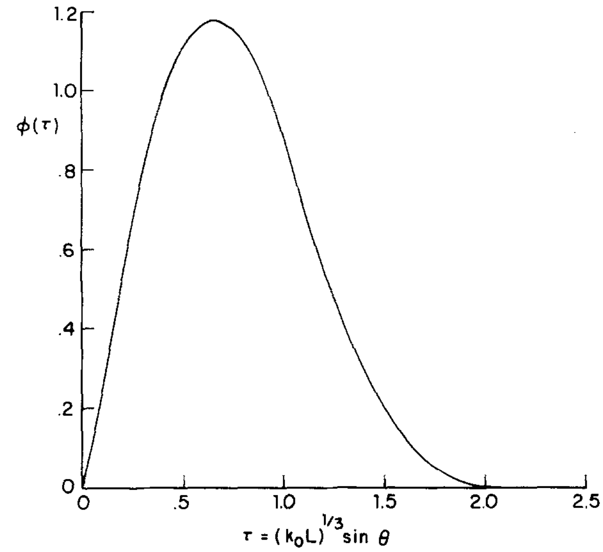

FIG. 1. Angular dependence of enhancement factor $\phi(\tau)$ in resonance absorption by a plasma of density-gradient scale length L.

known, however, that, at typical laser intensities, the ponderomotive force of the laser light can alter the plasma density profile,[10] leading to a weaker dependence of T_h on I. Self-consistent models of ponderomotive profile steepening[11] predict a scaling $T_h \propto I^\delta$, where δ lies in the range 0.31 to 0.39.

A question naturally arises as to how wave breaking, which produces an electron burst of a single energy ϵ_{br} each optical cycle, can lead to a broad suprathermal electron energy spectrum. It is tempting to reply that this is the result of averaging over the random distribution of spatial and temporal intensity fluctuations present in any real laser beam. However, Bezzerides *et al.*[12] have recently suggested that the assumption of such fluctuations is not necessary. Rather, they propose that a monoenergetic electron burst is indeed emitted every optical cycle, but that its energy fluctuates randomly from cycle to cycle, producing, after some time, the broad suprathermal tail seen in simulations. The randomness in the electron distribution comes predominantly from aperiodic Fourier components of the resonantly enhanced electric field, even with a constant and uniform laser intensity. One of the realizations to which we have come during the course of this work is that, under certain circumstances, there may not be sufficient time for self-consistent profile modification, or even for the statistical process of Ref. 12, to be effective. The latter process requires many optical cycles; for CO_2 laser light, it may take several psec or longer to build up a broad suprathermal tail out of individual monoenergetic electron bursts. Complete steepening of the plasma density profile by the ponderomotive force takes even longer, a considerable fraction of a cycle of ion plasma oscillation. For a critical-density D_2 plasma and CO_2 laser light, 40 psec or longer is required.[13] We believe that some of our experimental results reflect the dominance of a transient regime in which electron emission lasts only 1 to 2 psec. On such a short time scale, neither of the two steady-state mechanisms just mentioned is expected to be important; however, in Sec. V, we propose an unrelated transient mechanism which appears to explain our results quite well.

B. Structure of shock-front targets

The density structure of the shock fronts produced during these experiments has not been measured. However, as detailed in Sec. III, the experiments were carried out in a region of parameter space in which the actual shock-front structure is experimentally known to correspond to theoretical predictions. We review the experimental and theoretical results in this section.

The standard fluid-mechanical treatment of one-dimensional shocks is available in many texts. We intend only to quote well-known results[14] and to briefly outline the physical concepts involved. In such a treatment, the pressure, P_1, density ρ_1, and temperature T_1 in the cold gas ahead of the shock front are presumed known. There are four other parameters in the problem; namely, the Mach number M (the ratio of the shock-front speed to the sound speed $a_1 = (\partial P_1/\partial\rho_1|_s)^{1/2}$ and the thermodynamic variables P_2, ρ_2, and T_2 in the hot, dense gas behind the shock front. These seven variables are related by the three fluid equations, which express conservation of mass flux, momentum density, and specific enthalpy across the shock, and by the equation of state. Arithmetic reveals that there are not enough equations to close the system, so there must be one free parameter. It is convenient to choose the Mach number for this role, since it is easily measured experimentally. In terms of M, the system of equations yields the following relations for a shock wave in an ideal gas:

$$\rho_2/\rho_1 = M^2/(\mu^2 M^2 - \mu^2 + 1), \tag{4}$$

$$\frac{T_2}{T_1} = \frac{[\mu^2(M^2-1)+M^2][\mu^2(M^2-1)+1]}{M^2}. \tag{5}$$

Here, $\mu^2 = (\gamma - 1)/(\gamma + 1)$, where γ is the usual ratio of specific heats. For strong shocks ($M \to \infty$), we see that $\rho_2/\rho_1 \simeq \mu^{-2}$, independent of M; thus, shot-to-shot fluctuations in M have little effect on the shock-front density jump if the shock is sufficiently strong. For typical experimental shocks with $M = 5$ in D_2 at room temperature, Eq. (5) predicts that the highest temperature behind the shock is $kT_2 = 0.22$ eV. In this case, the Saha equation predicts that shock heating causes essentially no ionization,[15] and we observe this experimentally. Plasma is created in this experiment exclusively by optical breakdown.

The detailed density structure inside a shock front is of great importance in this work and has been the subject of much theoretical and experimental study. Shock structure cannot be calculated from fluid mechanics but requires a full, statistical treatment. We quote experimental results of Ahlsmeyer[16]: in argon, the density structure of a shock front may be expressed to within a few percent as

$$\rho(z) = \rho_1 + (\rho_2 - \rho_1)\tanh(z/L), \tag{6}$$

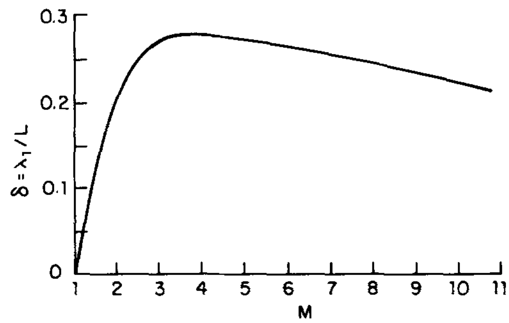

FIG. 2. Scaling of shock-front thickness L with Mach number M in argon (from Ref. 15). λ_1 is the mean-free path ahead of the shockfront, as defined in the text.

where ρ_1 and ρ_2 satisfy (4); z is the distance along the shock-tube axis. The shock thickness L is found to scale with the downstream (unshocked) mean-free path $\lambda_1 = (16/5)(\gamma/2\pi)^{1/2}(\eta_1/\rho_1 \alpha_1)$ (η_1 is the viscosity in the unshocked gas; $\gamma = 5/3$ in Ar) in a manner illustrated in Fig. 2. We see that, for $M \simeq 5$, L is about four mean-free paths and only weakly dependent on M. Thus, shot-to-shot fluctuations in M will have little effect on L. The curve in Fig. 2 has vertical error bars of a few percent.

These experimental results were obtained in Ar, a monatomic gas. In a gas of diatomic molecules, the shock structure is more complicated because the different molecular degrees of freedom relax at different rates; one may say that γ is a function of position in the shock front. In H_2 and D_2, however, the situation is simplified again: the rotational levels are widely spaced and are not thermally populated at room temperature. Thus, rotational relaxation lags far behind translational relaxation when the shock-front passes. This leads to the creation of two widely separated shock fronts[17] the first is due to translational relaxation alone and is described by Eqs. (4), (5), and (6) with $\gamma = 5/3$. The shock thickness L scales with M and λ_1 as in Fig. 2. The second front is due to rotational relaxation and can be described[17,18] as an exponential decay, with relaxation time τ, to the conditions given by (4) and (5) with $\gamma = 7/5$. This results in a rotational shockfront thickness $L_r \sim U\tau$, where U is the shock speed. $\tau \simeq 10$ nsec over a wide range in T_2.[17] Thus, in D_2, $L_1 \simeq 800$ μm, while the translational front thickness, for typical pressures used in this experiment, is one hundred times smaller. The rotational shock front plays no role in the present work.

From these experimental and theoretical results, we can calculate the density structure of an experimentally produced shock front with good accuracy. The density profile of a shock-front target produced under typical experimental conditions is shown in Fig. 3. The density-gradient scale length is typical 5–10 μm, and the upstream neutral-atomic density is slightly supercritical. The density-gradient vector lies parallel to the shock-tube axis. These features are well characterized theoretically and are expected to exhibit good experimental reproducibility.

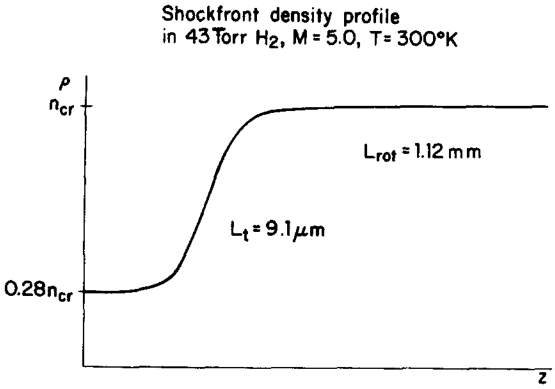

FIG. 3. Shock-front density $n(z)$ vs distance z along shock tube axis, for typical experimental parameters.

III. EXPERIMENTAL TECHNIQUES

A. Laser system

The CO_2 laser system used in these experiments consists of a single-mode, hybrid-TEA laser oscillator, followed by an optical-free-induction-decay pulse shaper,[19] followed by one of two TE laser amplifiers. The oscillator is grating-tuned to the P(20) CO_2 laser line and consists of a Tachisto model 215 discharge head and a cw intracavity low-pressure cell for single-longitudinal-mode operation. An intracavity aperture suppresses higher-order transverse modes. The single-mode output pulse has a duration 70 nsec FWHM and energy 700 mJ. The pulse passes into the free-induction-decay pulse shaper, which consists of a self-triggered plasma shutter,[20] a spatial filter, and an free-induction-decay cell.[21] The output of this system is an ultra-short pulse with a 10-psec rising edge and an exponentially decaying tail whose time constant can be adjusted to achieve pulse durations in the range 30–300 psec FWHM.[22]

In the "long-pulse" mode of operation, the free-induction-decay pulse is directed, double-pass through a Lumonics model 103 TE laser amplifier. This bandwidth-limited system produces a pulse of risetime 220 psec and duration 510 psec FWHM. The output pulse energy can be as high as 150 mJ; the peak-to-precursor energy contrast ratio can be several hundred.[21] The far-field intensity profile is very accurately Gaussian.[23]

In the "short-pulse" mode of operation, the free-induction-decay pulse is sent, double-pass, through a Lumonics model 282 TE, 10-atm laser amplifier. In this mode, the laser system produces an output pulse whose risetime is limited by the amplifier bandwidth and is estimated to be 20 psec. The time constant of the exponentially decaying tail can be adjusted to achieve durations in the range 100- to 200-psec FWHM. The achievable output pulse energy depends on the pulse duration and can be as high as 150 mJ for a 200 psec FWHM pulse. The contrast ratio can be as high as several hundred. The repetition rate of the laser system, in either mode of operation, is 16 shots per minute. The laser pulse can be synchronized to an external event with a jitter ±25 nsec.

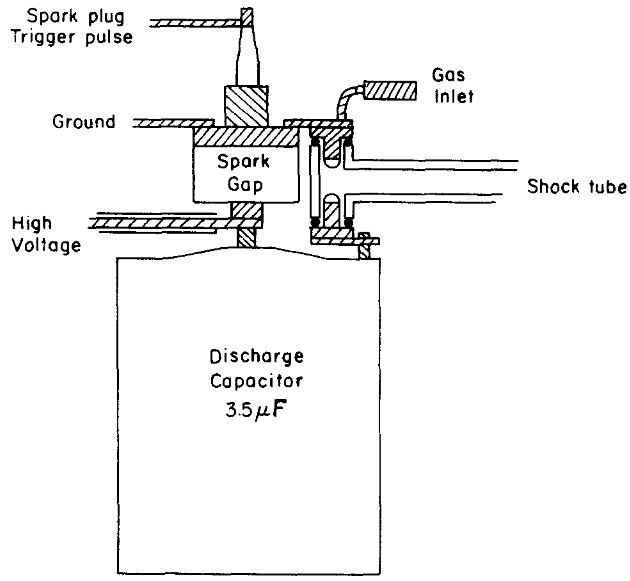

FIG. 4. Shock-tube discharge apparatus.

B. Shock-tube system

The shock tube is constructed of quartz tube of 12.7 mm i.d. and 3 mm wall thickness. The tube is 230 mm long and is joined in a Tee at one end to a 46 mm long section of the same tubing. Tungsten electrodes are soldered into copper plugs which are inserted into and seal against the two openings of the Tee; this results in an electrode spacing of about 10 mm. A spark gap discharges a 3.5 μF energy storage capacitor (Maxwell Laboratories, Inc.), charged to 10–12 kV, across these electrodes. This circuit is assembled into the compact unit sketched approximately to scale in Fig. 4. Not shown is the hand-wound charging inductor, plotted in epoxy and wired in parallel with the shock tube. Note that one of the electrodes is equipped with a gas inlet tube. Measurements of the discharge waveform are consistent with a circuit inductance of 65 nH and resistance of 20 mΩ. Assuming that half the discharge energy is lost in the spark gap, 20% of that energy should be dissipated in the shock tube during the first ring of the discharge. At 10 kV, the circuit can drive a shock with $M=5$ in 50 Torr H_2, consistent with energy balance at this efficiency.

The discharge apparatus is laid horizontally in a copper box, which provides electromagnetic noise shielding, protection from dangerous high voltages, and a duct for forced-air cooling by means of a fan. A pickup coil mounted in the roof of the box provides an electrical timing signal synchronous with the breakdown of the electrode gap. When connected to the rest of the gas-handling system, this apparatus can produce a Mach-5 shock in 50 Torr H_2 every few seconds. The shot-to-shot fluctuations in M are ±3% and are partially correlated with drifts in pressure and charging voltage. Very low levels of acoustic and electrical noise are produced.

The shock-front target for this experiment must have a sharp density gradient which is well-characterized and reproducible in both magnitude and orientation. It was shown in Sec. IIB that an ideal, planar shock does indeed have these properties. However, steps must be taken to assure that the acoustic disturbance generated in a real device, such as that just described, also satisfies these requirements. Operating at Mach numbers below 20 and at D_2 pressures above 1 Torr assures that the shock front is correctly described by the fluid-mechanical theory given in Sec. IIB and is unperturbed by ragged plasma "wisps"[24] or by turbulence.[25] At $M = 5$, the considerations of Sec. IIB imply that the density jump ρ_2/ρ_1 and the scale length L are only weakly affected by shot-to-shot fluctuations in M. All of the experiments described here were performed with $M = 5.0 \pm 4\%$.

The laser-interaction experiment is performed by irradiating the shock front as it reaches the end of the shock tube. The tube was made long enough to allow the laser focus to be placed at least 10 tube diameters away from the shock-tube discharge. This well-established practice[14] allows enough distance of travel for the complete formation of a sharp shock front. On the other hand, the tube is short enough so that the growth of boundary-layer drag along its length does not cause shock-front curvature to seriously affect the orientation or structure of the shock front near the shock-tube axis. In particular, the shock-front density-gradient vector, near the axis, is always parallel to it. Operation at pressures of 40–70 Torr produces shock thicknesses in the range 5–9 μm, which is an interesting one for the study of resonance absorption. Ionization of these targets is known to proceed via a fast laser-driven breakdown wave[7] which produces an inhomogeneous, overdense plasma with the same density structure as the shock front. In short, the shock tube produces a nearly ideal target for the study of resonance absorption.

The shock tube is connected to the rest of the experiment as shown in Fig. 5. An aluminum cell mates with the end of the shock tube and with a 2.54 cm focal-length lens. The axes of the shock tube and of the laser beam intersect at an angle of 30°, the optimum angle for resonance absorption by a density-gradient scale length 5 μm. The focus of the lens lies approximately in the plane of the wall of the cell and can be located, using a piece of burn paper mounted on a micrometer state, to within a few tens of μm.

All the experiments reported here were performed with an f/1 doublet lens (Laser Optics, Inc.) whose focal-spot diameter was $2\omega_0 = 17$ μm, and whose focal depth is calculated to be $z_0 = 21$ μm.

A portion of the CO_2 laser pulse is split off with a NaCl flat and focused onto a fast Ge:Au detector for pulse energy monitoring. The detector is calibrated during each run against a Scientech model 362 energy meter, which is accurate to $\pm 3\%$.

Experiments have been conducted on shock fronts in a variety of gases, including N_2, CH_4, He, H_2, and D_2. Of these, only D_2 has yielded a significant amount of useful data. Some results for H_2 will also be reported. During experimentation, a pump draws gas through a 75-Å Millipore filter and a liquid N_2 cold-trap, into the inlet tube shown in Fig. 4, down the shock tube, and out of the target chamber. The flow rate is set to assure that the shock tube is filled with fresh gas for each laser shot. This system reduces the concentration of low-ionization-potential impurities in the gas.

Due to the $\pm 3\%$ shot-to-shot fluctuations in the shock velocity, it is necessary to synchronize the laser pulse not just with the breakdown of the shock-tube discharge, but rather with the motion of the shock front as it travels toward the laser focus. This is accomplished by a two-channel laser-schlieren system which is illustrated in Fig. 5.

A HeNe laser beam is focused onto the axis of the

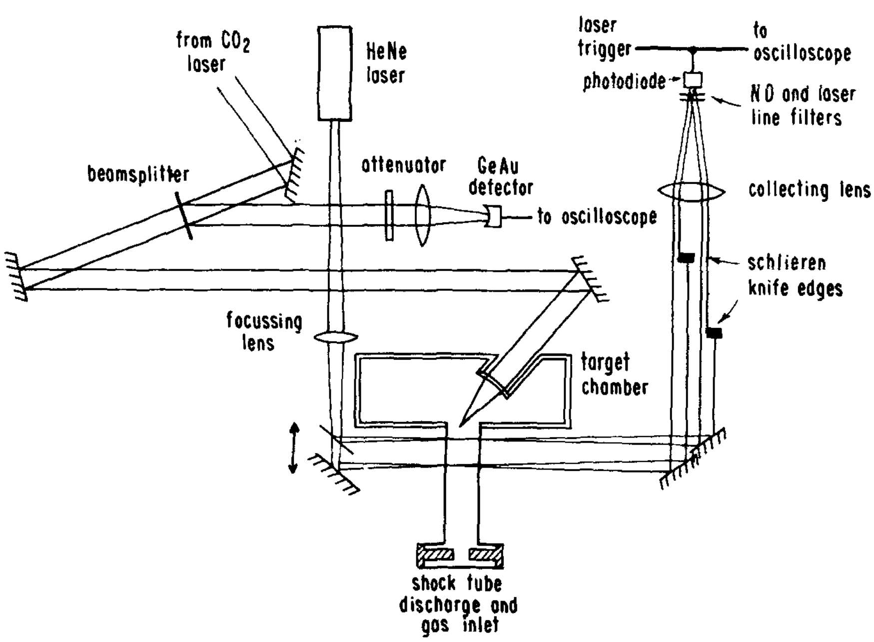

FIG. 5. Layout of experimental apparatus, showing laser-schlieren shock-front detection system.

shock tube at right angles to it. The beam is then directed to an RCA C30816 photodiode which is partially blocked by a knife edge. As the shock front passes through the focus, the rays of light are deflected in the direction of higher optical density; that is, past the knife edge and into the detector. A short output pulse results, which is used to trigger the laser. In the present arrangement, the 5 mW laser is split into two beams by a beamsplitter and mirror which can be independently moved parallel to the shock-tube axis. They are focused by a single lens onto a photodiode, which is shielded from stray light by HeNe laser-line filters and a neutral-density filter. This arrangement allows deduction of the shock-front velocity from the timing of the two photodiode output pulses. The CO_2 laser is triggered by the first pulse and ignores the second. Thus, the shock front must travel from the first laser beam it encounters to the CO_2 laser focus in the same time it takes the CO_2 laser pulse to arrive there. The Mach number can thus easily be set as desired by moving the first HeNe laser beam and adjusting the discharge voltage until synchronization is established.

Using the timing signals generated by the laser-schlieren system, the trajectory of the shock front can be estimated. The position of the shock front, at the instant that the CO_2 laser pulse arrives, can be determined from this calculation to within ± 75 μm.

C. Diagnostics

In addition to the laser pulse diagnostics and shock-front position determination just mentioned, measurements made during the course of these experiments include the following:

(1) *Background plasma characterization.* The plasma density and electron temperature in the gas in the target chamber were measured using biased charge collectors and Langmuir probes. Near the laser focus, uv photoionization by the shock-tube discharge produces a background plasma density $n_e \sim 10^{11}$ cm^{-3} and temperature $kT_e \lesssim 0.5$ eV. Impact ionization by the fast electrons emitted from the laser focus produces an electron density $n_e \sim 5 \times 10^{11}$ cm^{-3} along their path.

(2) *Total electron emission from the target.* As shown in Fig. 6, this is accomplished by an ORTEC Si surface-barrier detector which looks at the laser focus along the shock-tube axis. The detector is masked by a 13-μm aluminum foil; incident fast electrons come to a stop in the foil, producing Al k x rays which are sensed by the detector. The detector signal is sent to an ORTEC model 124 charge preamplifier whose output is read on a Tektronix 7904 scope. This system provides a time-integrated measurement of total emitted charge which is not absolutely calibrated. Time-resolved, absolutely calibrated measurements are made with a miniature, coaxially shielded, biased charge collector which is connected to the input of a Tektronix 519 oscilloscope. The time response is 300 psec.

(3) *Angular distribution of electron emission.* For this measurement, the Si surface-barrier detector in Fig. 6 is replaced by a small piece of Kodak No-Screen x-ray film, wrapped in 13-μm-thick Al foil. An image of the electron emission is created on the film by the Al k x rays produced when fast electrons are stopped in the foil.

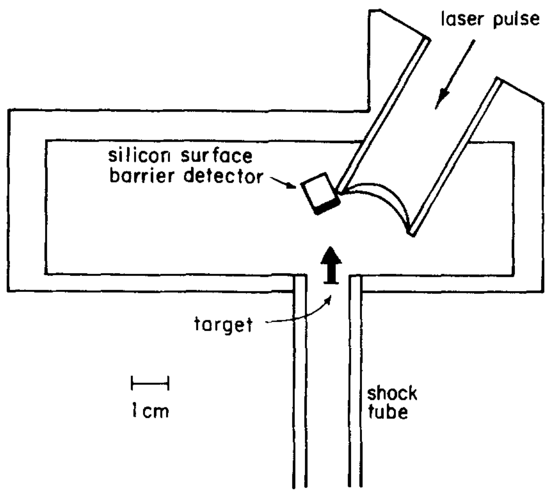

FIG. 6. Detail of target chamber showing positions of Si surface-barrier electron detector and CO_2 laser focusing lens. The target is shown in focus; the heavy arrow represents the direction of electron emission in resonance absorption.

(4) *Energy spectrum of electron emission.* Electrons produced by wave breaking are emitted from the target along the density-gradient vector, which, in this apparatus, is expected to lie parallel to the shock tube axis. This is indeed the case, as will be demonstrated in Sec. IV.

This quasi-unidirectional emission allows a magnetic spectrometer with reasonable focusing properties to be constructed. For this purpose, the target chamber is placed between the pole faces of a small permanent magnet, and a detector is placed in the focal plane, as shown in Fig. 7. The magnetic field strength was mea-

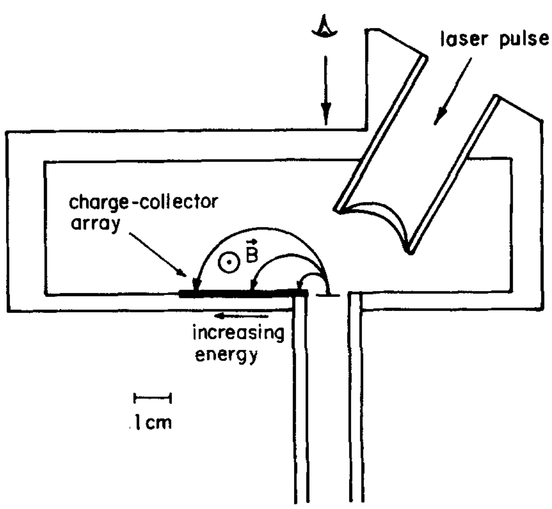

FIG. 7. Detail of target chamber showing spectrometer magnetic field lines and position of focal-plane charge-collector array.

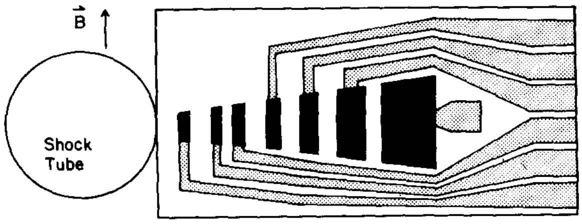

(a)

Channel	Average energy, keV	Energy width, keV
1	15.2	2.2
2	23.9	2.7
3	31.2	3.3
4	44.0	4.9
5	59.3	7.6
6	81.8	15.3
7	116.9	35.6

(b)

FIG. 8. Details of the spectrometer change collector array. a) View seen while looking down the shock-tube axis from the position of the "eye" in Fig. 7. (b) Parameters of the array used during these experiments.

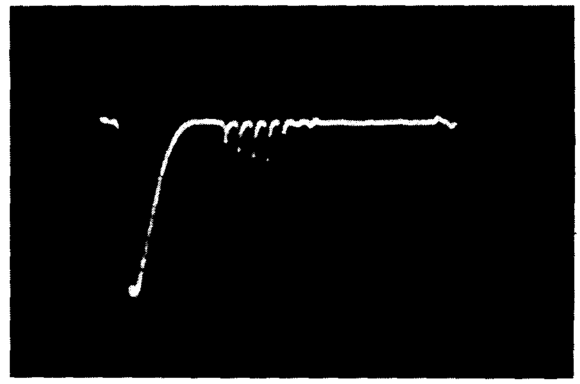

FIG. 9. Oscilloscope trace produced by irradiating a shock front with $M = 5.1$ in 57 Torr D_2 with a 100 psec-FWHM CO_2 laser pulse. Total trace duration is 100 nsec. The listed parameters of the electron energy spectrum determined by this trace were calculated as detailed in the text. $T_h = 27.3$ keV, $n_h = 3.7\times10^8$.

sured with a Hall probe to be within the range 760 G ± 40 G everywhere in the region in which detected electrons travel. The stopping power of the gas is calculated to have a negligible effect on the trajectories of the detected electrons in the magnetic field.

An array of charge collectors is placed in the focal plane of the spectrometer. A view of these, as seen by looking along the axis of the shock tube from the position of the eye in Fig. 7, is sketched in Fig. 8(a). These consist of copper pads etched onto a printed circuit board and are colored black in the drawing. The expanding shape of the array automotically compensates for the fact that electron emission from synchronized shock fronts is from the laser focus into a cone. Each collector is heavily tinned to assure that the incident electrons are stopped in the conductor. The energy width of each collector was chosen to be 30% of its center energy, so as not to exceed the geometrical resolution of the spectrometer, which is largely determined by magnetic field inhomogeneities and the finite cone angle of electron emission. Since the energy spectrum is bound to fall off at higher energies, this geometry enhances the signal due to high-energy electrons, resulting in wide dynamic range. The values used are tabulated in Fig. 8(b). The collectors are connected, via paths on the circuit board shown in grey, to individual miniature coaxial cables which lead out of the target chamber. The whole circuit board, except for the triangle area occupied by the collectors, is covered with Plexiglas and wrapped in 100 μm thick copper foil, which is soldered to the shields of the cables. Thus, signals can only result from charged particles striking the collectors. When the shield is properly grounded to the target-chamber wall, there is no measurable inductive interaction with the chamber, and very clean signals result.

Data are acquired by attaching all the collectors to the same oscilloscope input, by cables of different lengths. The signals arrive in sequence, and a spectrum is displayed on a single oscilloscope trace. In the typical shot shown in Fig. 9, the initial, broad peak is the CO_2 laser signal. The Ge:Au detector is filtered and integrated to provide this measure of the laser pulse energy. Following this are signals from the last five spectrometer channels, appearing in sequence at 9 nsec intervals, starting with the highest energy channel. These pulses are integrated by the 225-MHz oscilloscope preamp bandwidth, so that their heights are proportional to the total collected charge. Reflections from the improperly terminated oscilloscope input are arranged to follow the signals, by the use of very long cables. The signals I_i from the last four spectrometer channels ($i = 4, 5, 6, 7$) are found to approximately obey a relation of the form

$$I_i = N_h \exp(-\epsilon_i/kT_h)\Delta\epsilon_i, \quad i = 4, 5, 6, 7, \tag{7}$$

where the center energies ϵ_i and energy widths $\Delta\epsilon_i$ are tabulated in Fig. 8(b). A least-squares fit of this form, applied to the first four peaks in Fig. 9, yielded a hot-electron "temperature" $kT_h = 27.3$ keV and "number" $n_h \equiv N_h kT_h = 3.7\times10^8$. These values are quite typical.

The calibration of the spectrometer was checked by covering the charge collectors with plastic and metal foils of varying thicknesses, followed by exposure to resonance electron emission from properly focused shockfront targets. The effects of the foils on the spectrometer signals were correctly predicted by calculations based on the stopping powers of the foils.[26] Total spectrometer accuracy is ± 15%.

Charge collector artifacts may be caused by electrons liberated by the photoelectric effect or by emission of secondary ions or electrons, but one expects these to be of such low energies (< 100 eV) as to be confined, by the spectrometer magnetic field, to their place of origin. Applying a bias voltage to the charge collectors has confirmed this expectation: Varying the bias over the range ± 500 V has never produced any effect in the measured spectrum or in the fast (1 nsec) signals from any charge collector placed anywhere in the target chamber.

IV. EXPERIMENTAL RESULTS

A. General results and overview

To test the crucial assumption that the presence of a shock front in the laser focus should make the laser-plasma interaction reproducible, we studied the total electron emission from shock-front targets as a function of shock-front position. The electrons were detected with the Si surface-barrier detector mounted as in Fig. 6. Figure 10 shows the resulting signal plotted as a function of shock-front position with $M=4.8$ in 43 Torr D_2 (Δx is the distance, measured along with the shock-tube axis, between the shock front and the laser focus). The data in Fig. 10 were produced with 500-psec-FWHM laser pulses whose energies lay in a ±20% range. This graph has a simple interpretation. The points on the left of the graph ($\Delta x<0$) result from shots in which the shock front had not yet reached the laser focus when the laser pulse arrived ("late" shock fronts). The breakdown thus took place in 43 Torr D_2, in which even total ionization could not produce the critical density needed for resonance absorption. No signal was produced. On the right of the graph ($\Delta x>0$), the breakdown took place in the overdense gas behind an early shock front. The shock front found itself in a region of weak laser intensity and played no role. Its position was irrelevant, and the signal strength was similar to that produced in an unshocked, homogeneous gas.[7] But, when the shock front was in correct focus ($\Delta x=0$), the signal was enhanced by a factor of 10. This is the signature that the experiment works as planned.

Other evidence for the conclusion that the presence of a shock front in the laser focus has a profound effect on the laser-plasma interaction comes from measurements of the angular distribution of electron emission. For this experiment, the Si detector was replaced by a piece of x-ray film wrapped in Al foil. The results are not completely unambiguous, because, due to the ±3% shot-to-shot fluctuations in shock-front speed, each film is likely to be exposed to many out-of-focus shock fronts for each property focused one. Nonetheless, honest conclusions can be drawn from the patterns of exposure on the film. Two such films are shown in Fig. 11. Here, the films are presented as seen by the target. The plane of polarization intersects each film in a horizontal line which passes through the center of the spot of exposure. The upper film was produced in a homogeneous gas and is included for comparison. Here, unreproducible emission into a wide range of angles is seen, as described in a previous publication.[7] Early shock fronts produce similar patterns of exposure. Late shock fronts produce no exposure. As seen in the lower film, however, properly focused shock fronts emit electrons predominantly in a cone of half-angle 20°–25°, centered on the shock-tube axis.

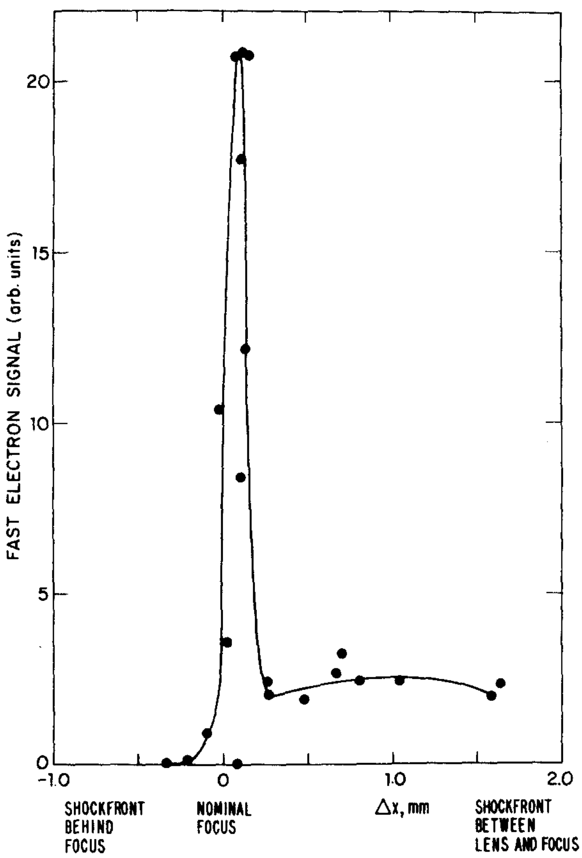

FIG. 10. Electron signal vs shock-front position Δx for a shock shock front of strength $M=4.8$ in 43 Torr D_2, irradiated with 500 psec laser pulses.

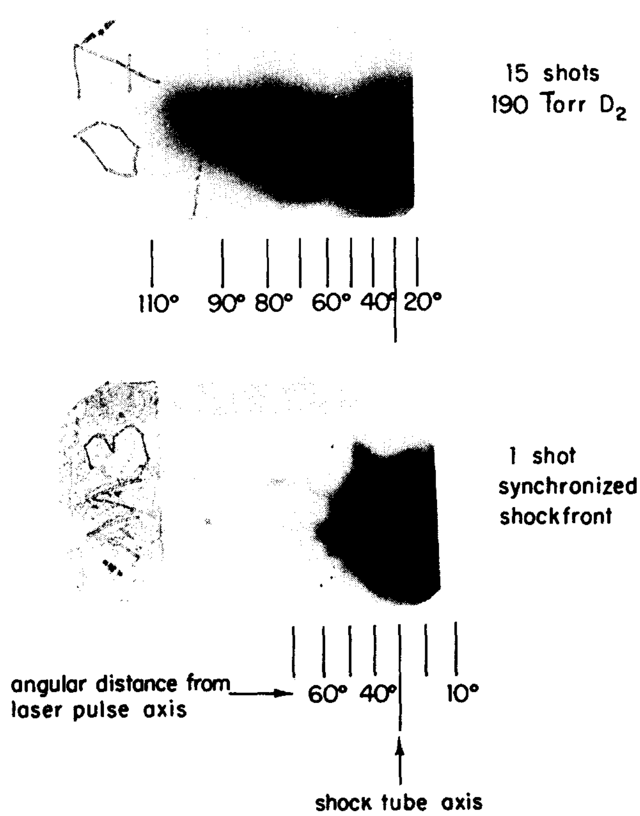

FIG. 11. X-ray film exposure by electrons emitted by homogeneous gaseous targets (top) and by a properly focused shock-front target of strength $M=4.8$ in 43 Torr D_2 (bottom).

Since electrons are emitted along the plasma density-gradient vector, this observation proves that this vector coincides with the neutral shock-front density-gradient vector, which is known to lie along the shock-tube axis. The angular spread can easily result from bulging of the otherwise flat target due to hydrodynamic expansion, or from the existence of a rippled critical surface.[27]

Taken together, these observations confirm the main assumption on which this experiment rests: the orientation of the critical surface is made reproducible by using a shock front for a target.

The observation of an emission cone of half-angle 25° implies that the electron spectrometer sketched in Fig. 7 can have an energy resolution ±15%. One of the earliest spectra obtained with this device is reproduced in Fig. 12. A shock front in 43 Torr D_2 was irradiated with a single, 100-mJ, 500-psec laser pulse to produce this spectrum. The dark bars along the horizontal axis represent the energy widths of the charge collectors. The vertical positions of the data points are calculated by dividing the signal from each charge collector by its energy width. This spectrum exhibits a typical bi-Maxwellian shape with a poorly defined cold electron temperature, kT_c, of perhaps 2 keV, and an easily discernible suprathermal tail with $kT_h = 36$ keV. Our general observations about such spectra can be summarized as follows:

(1) The total number $\int_0^\infty N(\epsilon)d\epsilon$ of emitted electrons, as measured with the calibrated change collector mentioned in Sec. III, is space-charge limited, in accordance with the Langmuir–Child law.

(2) The spectral shape below $\epsilon = 40$ keV is not reproducible from shot-to-shot.

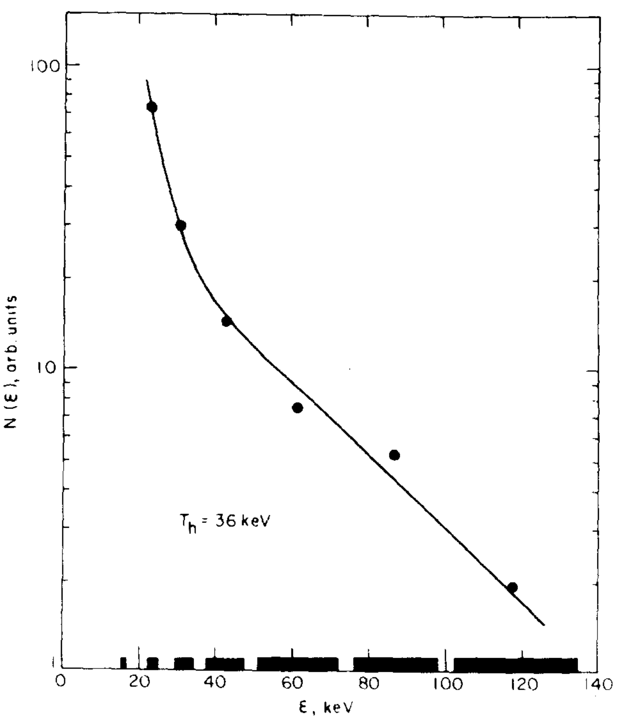

FIG. 12. A typical electron energy spectrum $N(\epsilon)$ vs ϵ.

(3) The temperature, T_h, of the suprathermal tail above 40 keV, as obtained from the least-squares fit of Eq. (7), is quite reproducible and is typically 20 to 35 keV, depending on experimental parameters.

(4) The integrated number of hot electrons, $n_h \equiv N_h kT_h$, as obtained from (7), is typically 0.3 to 3×10^9 and fluctuates over an entire order of magnitude from shot-to-shot.

(5) The total hot-electron energy, $\epsilon_{tot} \equiv n_h kT_h$, is typically 10^{-4} of the laser pulse energy.

We believe that the fluctuations noted in observations (2) and (4) are the result of time-varying space-charge limitations, but that the observed hot-electron temperature, T_h, is actually the same as is created inside the target. Our reasoning is as follows: suppose the electrons are created in the target with an energy spectrum $N_{cr}(\epsilon)$. If they are emitted at a time-varying rate $R(t)$, and if the space-charge potential on the target is $\phi_p(t)$, then the observed spectrum will be

$$N(\epsilon) = \int_0^\infty dt\, R(t) N_{cr}[(\epsilon + e\phi_p(t)]\,. \tag{8}$$

If we consider only the high-energy tail of the spectrum, then we can make the approximation

$$N_{cr}(\epsilon) \simeq \eta_{cr} \exp(-\epsilon/kT_n)\,. \tag{9}$$

Thus, the tail of the observed spectrum has the shape

$$N(\epsilon) \simeq \int_0^\infty dt\, R(t)\eta_{cr} \exp\left(\frac{-(\epsilon + e\phi_p(t))}{kT_h}\right) = A\eta_{cr} \exp(-\epsilon/kT_h)\,, \tag{10}$$

where

$$A = \int_0^\infty dt\, R(t) \exp[-e\phi_p(t)/kT_h]\,. \tag{11}$$

A is not a function of ϵ. Thus, the tail of the observed spectrum has the same T_h as that of the spectrum inside the target, despite the time-varying space-charge potential and emission rate. However, the amplitude of the tail of the observed spectrum, and thus n_h, is proportional to A, which is extremely sensitive to shot-to-shot fluctuations in the behavior of $\phi_p(t)$.

In the low-energy part of the spectrum, approximation (9) is not valid; thus, the spectral shape in this region is also affected by fluctuations in $\phi_p(t)$. These come about as low-energy electrons adjust their emission self-consistently, so as to satisfy the Langmuir–Child law. We estimate that, because of photoionization of the gas in a 200 μm radius sphere surrounding the target, ϕ_p reaches only 20 kV after 3×10^9 electrons are emitted.

These considerations have been applied to observations made using 500-psec FWHM laser pulses. They do not appear to be valid for results obtained with pulses of extremely short rise time (20 psec). This issue will be taken up in Sec. VB.

Table I is a brief summary of experimental results obtained in D_2 and H_2. In three of the four cases listed, there are enough data to determine a least-squares fit of the form $T_h \propto E_p^\delta$, where E_p is the laser pulse ener-

TABLE I. Summary of experimental conditions and data obtained with properly focused shock-front targets.

Gas	Pressure range (Torr)	Mach number	Laser pulse duration (psec)	Typical peak intensity ($\times 10^{14}$ W/cm^2)	Number of synch. shots	T_h, avg. (keV)	n_h, avg. ($\times 10^9$) [a]	η_h, avg. ($\times 10^{-4}$) [a,b]	Scaling exponent [c]
D_2	36–43	4.8	500	0.8	45	24.7 ± 12%	2.8	2.0	0.32 ± 0.03
D_2	48–67	5.1	200	1	20	29.1 ± 11%	2.6	1.7	0.08 ± 0.08
D_2	43–67	5.1	100	2	62	26.9 ± 7%	1.7	1.9	0.12 ± 0.1
H_2	43–45	5.1	100	2	9	27.1 ± 5%	1.1	1.2	···

[a] Geometric mean of all data.
[b] $\eta_h = n_h k T_h / E_p$, the fractional conversion of laser energy to hot electrons.
[c] Scaling exponent δ defined by least-squares fit of form $T_h \propto E_p^{\delta}$, with the pressure dependence scaled out as detailed in the text.

gy. These values of δ are listed in the last column of Table I, where a striking difference between 500-psec-FWHM laser pulses ($\delta = 0.32$) and shorter pulses ($\delta = 0.1$) is evident. The very low value of δ for the shorter pulses appears to be a consequence of the dominance of a regime of transient, monoenergetic hot-electron emission. By contrast, 500-psec-FWHM pulses allow the establishment of a steady state in which electron production is dominated by ponderomotive profile modification, which produces $\delta = 0.32$. These two cases will now be discussed separately.

B. Results with 500-psec-FWHM laser pulses

Data were acquired, with 200-psec-risetime, 500-psec-FWHM laser pulses, at pressures of 36, 39, 40, and 43 Torr D_2. For each pressure, a least-squares fit of the form $T_h \propto E_p^{\delta}$ yielded values of δ in the range 0.26–0.46. The pressure dependence of the average value of T_h [defined as the value of the least-squares fit $T_h(E_p)$ at $E_p = 65$ mJ] is shown in Fig. 13. This pressure dependence is evident even in the raw data but is not easily interpreted. Rather, our attention is focused on the dependence of T_h on E_p, by scaling the data to the value at 43 Torr. This is done by normalizing all the data at a particular pressure to the average value at 43 Torr (26.7 keV). With the pressure thus scaled out, all the data were used to produce a least-squares fit of the form $T_h = E_p^{\delta}$. The result is shown in Fig. 14 (here, the data have been averaged in groups of three to thirteen shots to make the graph neater). A least-squares fit to the points in Fig. 14 yields $\delta = 0.32 \pm 0.03$.

C. Results with 100 and 200 psec FWHM laser pulses

The 20 psec risetime laser-pulse data were acquired in D_2 and H_2 at pressures ranging from 43 to 67 Torr.

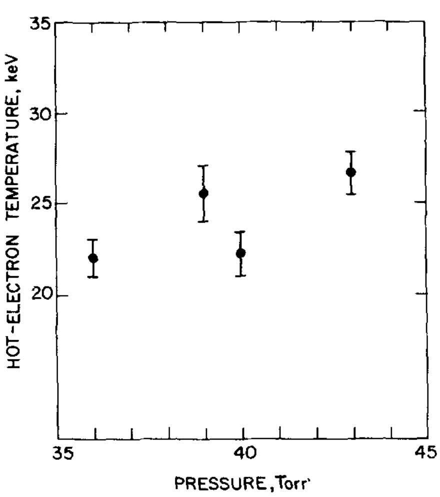

FIG. 13. Pressure dependence of the average hot-electron temperature, T_h, produced by $M = 4.8$ shock fronts in D_2 irradiated by 65-mJ, 500-psec-FWHM CO_2 laser pulses.

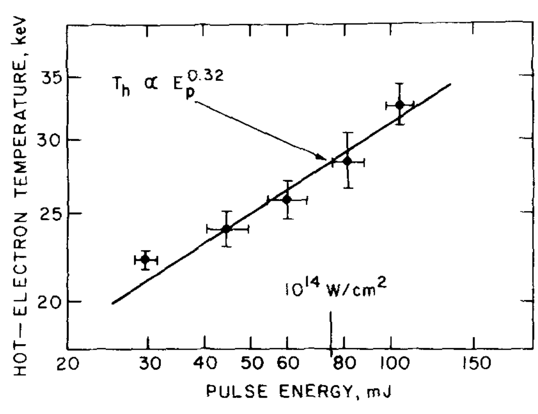

FIG. 14. Pressure-scaled hot-electron temperatures produced by $M = 4.8$ shock fronts in 43 Torr D_2 irradiated with 500-psec-FWHM laser pulses, plotted as a function of laser pulse energy, E_p. To improve the statistics, results obtained at other shocktube pressures have been averaged in, after normalization to the average value obtained at 43 Torr. In this figure and in Figs. 16 and 17, a tick mark is provided on the horizontal axis to calibrate the measured laser pulse energy with calculated peak laser intensity.

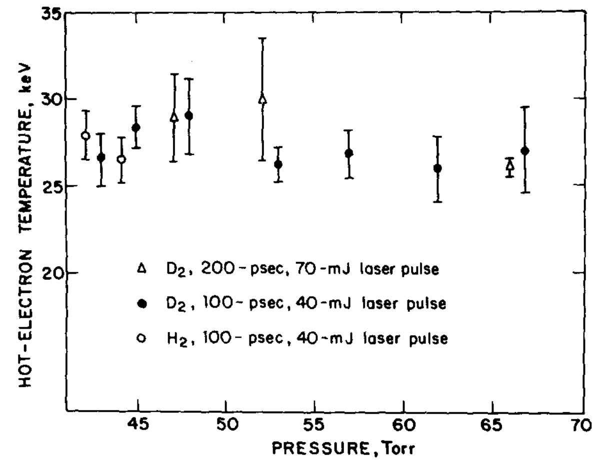

FIG. 15. Pressure dependence of the average hot-electron temperature produced by $M = 5.1$ shock fronts in D_2 and H_2 irradiated with 100- and 200-psec-FWHM laser pulses. The open circles and triangles have been displaced 0.8 Torr to the left for clarity.

For each gas, pressure, and pulse duration, the variation of the data with pulse energy was interpolated to a particular peak laser intensity, to yield an average hot-electron temperature. The variation of these values of T_h with pressure, for a peak laser intensity of 2.6×10^{14} W/cm^2, is shown in Fig. 15. For clarity, the data points for H_2 and for 200-psec laser pulses are displaced to the left by 0.8 Torr on this graph. The three experimental conditions produced hot-electron temperatures which are mutually consistent and which show essentially no dependence on pressure. Later, it will be useful to write $T_h \propto p^{\gamma}$; these data imply $\gamma = 0 \pm 0.5$.

The dependence of hot-electron temperature on 100

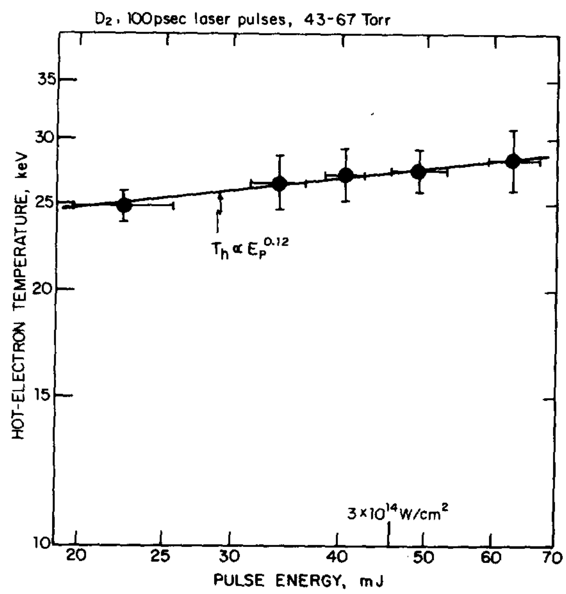

FIG. 16. Pressure-averaged hot-electron temperatures produced by $M = 5.1$ shock fronts in D_2 and H_2 irradiated with 100-psec-FWHM laser pulses, plotted as a function of laser pulse energy, E_p.

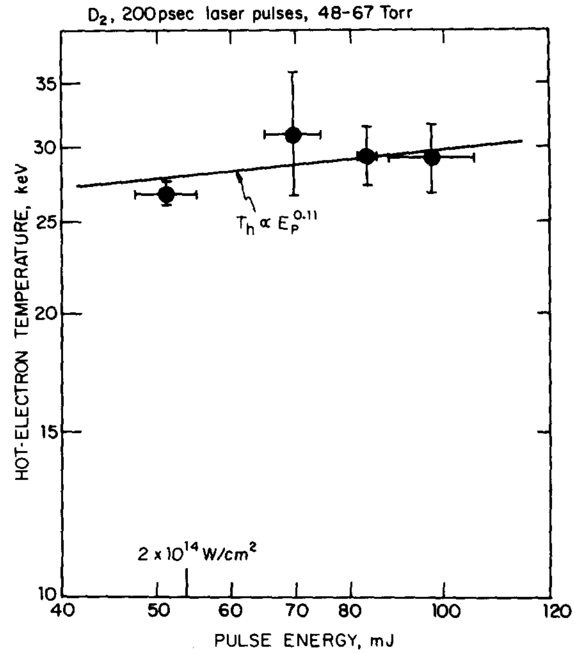

FIG. 17. Average hot-electron temperature vs laser pulse energy for $M = 5.1$ shock-front targets in D_2 and 200-psec-FWHM laser pulses.

psec FWHM laser-pulse energy is shown in Fig. 16. Here, data from all pressures were averaged together and fitted to a function of the form $T_h \propto E_p^{\delta}$. This procedure yielded $\delta = 0.12 \pm 0.1$. For 200 psec FWHM data, shown in Fig. 17, one finds $\delta = 0.08 \pm 0.08$.

V. DISCUSSION OF HOT-ELECTRON TEMPERATURE MEASUREMENTS

A. 500 psec FWHM laser-pulse results

The basic result obtained with 500 psec FWHM laser pulses is that the hot-electron temperature, T_h, scales with laser pulse energy, E_p, as $T_h \propto E_p^{0.32}$, in the intensity range $I\lambda^2 \sim 10^{16}$ W-μm^2/cm^2. This is in agreement with predictions of the model of ponderomotive profile steepening, and there is every reason for this to be so: Extrapolation of the avalanche-ionization scaling laws[28] indicates that a critical surface is first formed, on the high-density side of the shock front, approximately 50 psec after the start of a laser pulse of typical energy. The threshold for strong profile modification,[11] $I \sim 10^3$ W/cm^2, has already been exceeded at this time. The resonance interaction lasts for another approximately 50 psec until the low-density side of the shockfront is ionized, which cause the laser light to be refracted away from the target. By the estimates of Sec. II, this leaves enough time for strong profile modification. However, this is not enough time for significant distortion of the planar shape of the critical surface by motion at the ion-sound speed (the plasma electron temperature has been measured under similar circumstances[29] to be approximately 1 keV). So, the hot-electron energy spectrum produced by 500 psec FWHM laser pulses appears to be determined by profile steepening by the ponderomotive force.

B. Results with 100 and 200 psec FWHM laser pulses

Results obtained with 20 psec lifetime laser pulses are more difficult to explain. There are three basic experimental observations:

(1) 100 and 200 psec FWHM laser pulses yield similar results;

(2) H_2 and D_2 behave identically; and

(3) the dependence on experimental parameters is extremely weak; i.e., $\delta = 0.1 \pm 0.1$ and $\gamma = 0 \pm 0.5$.

This last observation is particularly troublesome, because it is predicted neither by the theory of strong profile modification ($\delta = 0.31$ to 0.39; $\gamma = 0$) nor by the assumption that the plasma density profile is the same as that of the un-ionized shock front ($kT_h = \epsilon_{br} \propto I^{1/2}L^{1/2}$, or $\delta = 0.5$; $\gamma = -0.5$). However, all of these observations can be explained by a model, one of whose predictions is that, at the laser intensities encountered in these experiments, the resonant laser-plasma interaction is finished before the peak of the laser pulse. The 100 and 200 psec FWHM laser pulses produced by the optical free induction decay system have identical 20 psec risetimes. Differences between these two pulses are made up in the tail, which does not participate in resonance absorption. Thus, observation (1) is expected. Furthermore, during the 20 psec risetime, hydrodynamic differences between D_2 and H_2 do not have time to manifest themselves, explaining observation (2). Finally, this time scale is also insufficient for ponderomotive profile steepening to become important; that would take 40 psec. In this case, then, the actual plasma density profile is determined by the progress of the breakdown wave which propagates through the laser focus. It appears that the electrons collected in this experiment are produced well before the steep part of the shock front is completely ionized. Its pressure-dependent structure is therefore not of great importance, even in the absence of profile modification. A weak dependence of T_h on pressure is therefore not entirely unexpected.

Furthermore, consider the propagation of the ion-

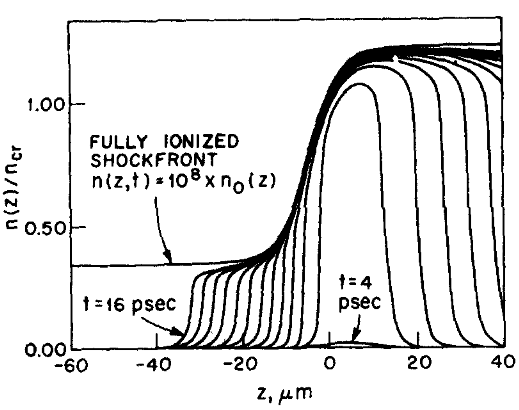

FIG. 18. Calculated plasma density, $n(z)/n_{cr}$, vs distance, z, for a shock front with $M = 5.1$ in 53 Torr D_2 irradiated by a 20-psec-risetime laser pulse of energy 100 mJ. The different profiles are separated in time by 1 psec.

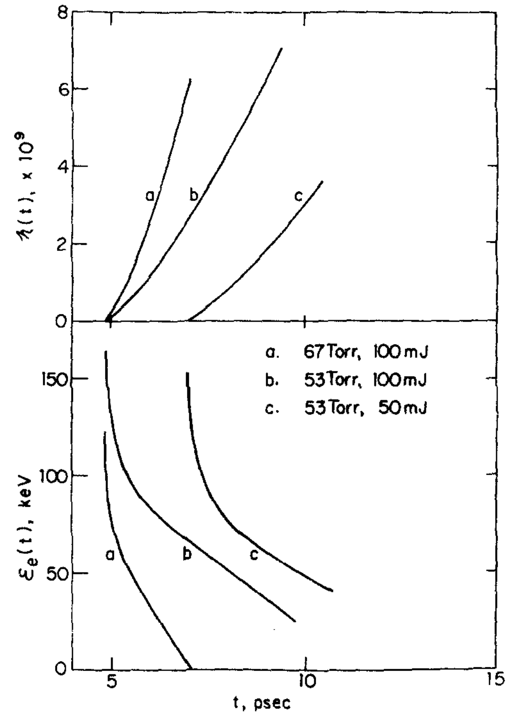

FIG. 19. Calculated integrated number, $\eta(t)$ (top) and emitted energy, $\epsilon_e(t)$ (bottom), of electrons emitted by shock fronts irradiated by 20 psec risetime laser pulses, versus time.

ization front during optical breakdown of a shock front by a laser pulse of energy E_p. This is sketched in Fig. 18. The plasma density structure is swept through a family of curves as time increases. The energy of fast electrons emitted at a particular time depends on the density structure and the laser intensity at that time. Now, if a different laser pulse energy is used, the density structure is swept through the same family of curves; only the time scale of the sweep is different. Similarly, the hot electron energy is swept through the same values as before, only on a different time scale. The actual spectrum of those energies will be seen to be affected very little by changing the laser pulse energy. In other words, T_h should depend only very weakly on E_p, as is seen experimentally.

The results of a numerical calculation of this model are shown in Fig. 19. Here, the energy, $\epsilon_e(t)$, and integrated number, $\eta(t)$ of emitted electrons are plotted as a function of time for three typical experimental conditions. It has been implicitly assumed here that the electron emission is monoenergetic at each instant in time. Electron emission starts when a critical density is first produced, 5–7 psec after the start of the laser pulse. At that time, the scale length in the critical layer is very long, and ϵ_e is large. It then decreases as underdense plasma builds up ahead of the critical layer, as in Fig. 18. Eventually, as $\epsilon(t)$ increases, $\epsilon_e(t)$ is reduced by the buildup of space charge on the target. Emission stops when $\epsilon_e(t) = 0$. The important thing to note in this figure is that, for electrons collected in this experiment ($\epsilon_e > 40$ keV), the curves have similar shapes for all experimental conditions. The time-integrated energy spectra of electrons emitted as in Fig. 19 depend on experimental conditions only through the shapes of the curves plotted there. Thus, the hot-electron temperatures assigned to these spectra should depend only weakly on E_p and p. This is as observed experimentally.

The basic physics of this model is that electron emission is a transient phenomenon. In Fig. 19 observe that the electrons collected in the experiment are emitted during a period of only 1 or 2 psec duration which begins at the first instant that a critical density is produced in breakdown. The 30 to 60 optical cycles may not be enough time to construct a complete bi-Maxwellian energy spectrum by random processes,[12] so electrons are emitted in a stream that is monoenergetic at each instant (by contrast, wave breaking takes only a few optical cycles[2]). The observed spectrum comes from the temporal variation of the energy of that stream, which in turn is due to the rapidly changing density profile of Fig. 18 and, to a lesser extent, to the buildup of space charge on the target.

This transient regime is unimportant for 500 psec laser pulses. For these longer pulses, breakdown occurs at much lower laser intensities; thus, electrons emitted at the instant of breakdown have very low energies and are stopped by only a modest buildup of space charge. Later in the pulse, higher laser intensities produce more energetic electrons over a period of perhaps 50 psec in duration. This is more than enough time for the formation of a complete bi-Maxwellian spectrum and for profile steepening by the ponderomotive force.

The numerical calculation of this model begins with the computation of the plasma density profiles $n(z,t)$ produced by a laser pulse of intensity $I(t)$, as shown in Fig. 18. Formulae from the theory of resonance absorption then yield the energy $\epsilon_{br}(t)$ and integrated number $\eta(t)$ of wave breaking electrons. The target builds up a space-charge potential $\phi_p(t)$ proportional to $\eta(t)$; the emitted electron energy is thus $\epsilon_e(t)=\epsilon_{br}(t)-e\phi_p(t)$. From this, a spectrum $N(\epsilon)$ is determined and its properties studied.

The plasma density $n(z,t)$ is assumed to vary in only one dimension. The initial density profile $n_0(z)$ is created by the flash of the shock-tube discharge. $n_0(z) \sim 10^{11}\ \mathrm{cm}^{-3}$ and has the structure of the shock front as discussed in Sec. IIB. The laser pulse causes avalanche ionization, producing a time-dependent density profile

$$n(z,t)=n_0(z)\exp\left(\int_0^{\infty}\eta(z,t')dt'\right). \tag{12}$$

In this calculation, total ionization is defined by $n(z,t) = 10^8 n_0(z)$. The ionization rate, $\eta(z,t')$, is given by the scaling law[28]

$$\eta(z,t')=f[E(z,t')]\tilde{n}(z,t'), \tag{13}$$

where $E(z,t')$ is the effective electric field of the laser, and $\tilde{n}(z,t')$ is the density of ionizing collision partners. The ionization rate depends dominantly on the initial density of neutrals, so it is assumed that

$$\tilde{n}(z,t)=\begin{cases} n(z,0), & \text{until ionization is complete;} \\ 0, & \text{thereafter.}\end{cases} \tag{14}$$

f is a function only of $E(z,t')$ at the low pressures encountered here, and it is assumed that $f\propto E^2$; i.e., that

$$\eta(z,t')=\alpha I(z,t')\tilde{n}(z,t'), \tag{15}$$

where $I(z,t')$ is the laser intensity. At the high electric fields encountered in this experiment, the kinetic energy of the oscillating electrons is much higher than the ionization potential of the molecules, so this is a good assumption [scaling the results to a measured breakdown threshold makes the exact form of (15) unimportant anyway].

With these assumptions, (12) and (13) yield

$$n(z,t)=n_0(z)\exp[\alpha E_p(z,t)\tilde{n}(z,t)], \tag{16}$$

where

$$E_p(z,t)=\int_0^t I(z,t')dt'. \tag{17}$$

Given a shock structure $n_0(z)$, a laser pulse shape $I(z,t)$, and a breakdown threshold (which determines α), Eq. (16) can be solved numerically, using (14) and (17). The result, for a 100 mJ, 100 psec FWHM laser pulse incident on a shock front of strength $M=5.1$ in 53 Torr D_2, was shown in Fig. 18. There, the laser was focused, with $z_0=21\ \mu$m, on the critical surface; i.e., where $n_0(z)=10^{11}\ \mathrm{cm}^{-3}$. To make it easy to distinguish the different curves in Fig. 18, the density $n(z,t)$ was artificially given a "softer saturation" than (14). This was not done in subsequent calculations; the effect of doing so is small anyway. In this calculation, breakdown is essentially complete before the peak of the laser pulse. The ionization front is seen to expand along the axis of the shock front with a velocity 3×10^8 cm/sec, in agreement with experimental observations.[30]

Using plasma density profiles as just determined, resonance absorption and wave breaking can be included to yield the hot-electron energy spectrum. This should be done by integrating Maxwell's equations with $n(z,t)$ as calculated here and then applying formula (3) to obtain the energy of emitted electrons. Given the limited accuracy of this calculation, however, it is far simpler to approximate the profiles $n(z,t)$ in Fig. 18 as linear density ramps of scale lengths

$$L_t(t)=\frac{2}{n_{cr}}\int_{-\infty}^{z_{cr}} n(z,t)dz, \tag{18}$$

where z_{cr} is determined by $n(z_{cr},t)=n_{cr}$. For a linear ramp of scale length L, (18) gives $L_t(t)=L$. This tunneling length is inserted into Eq. (1) to estimate the driving field E_d in the critical layer. With E_d and the local critical-layer density-gradient scale length

$$L_{br}(t)=n_{cr}\left(\left.\frac{dn(z,t)}{dz}\right|_{z=z_{cr}}\right)^{-1}, \tag{19}$$

Eq. (3) can yield the wave breaking energy $\epsilon_{br}(t)$.

The number, $\eta(t)$, of emitted electrons is calculated by assuming that all of the laser energy absorbed in a

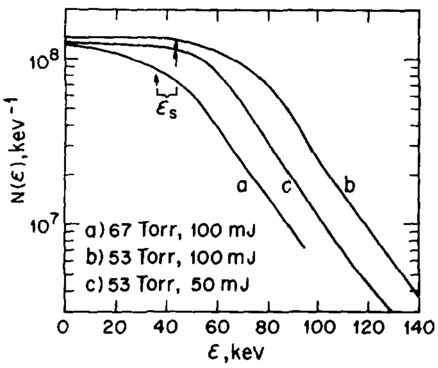

FIG. 20. Energy spectra of electrons emitted as in Fig. 19. ϵ_s is an approximate indication of the energy at which the spectrum starts to fall off in a suprathermal tail.

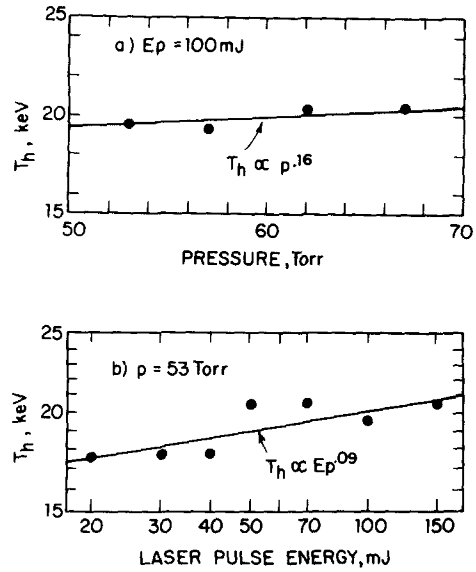

FIG. 21. Calculated scaling of hot-electron temperature T_h with (a) shock-tube pressure, p, (b) laser pulse energy, E_p.

particular time interval at time t is converted into electrons of energy $\epsilon_{br}(t)$. The absorption fraction, f_{abs}, was set at 10% to produce Fig. 19. As will be discussed later, the value of f_{abs} has practically no effect on either the hot-electron temperature or the total integrated number of emitted electrons; note, however, that $\eta(t) \propto f_{abs}$. The effect of space charge on the electron emission was included by subtracting from $\epsilon_{br}(t)$ the energy, $e\phi_p(t)$, left on a 200 μm radius sphere by the removal of $\eta(t)$ electrons. [Note, then, that $\phi_p(t) \propto f_{abs}$; f_{abs} may be regarded as a free parameter which adjusts the strength of space charge, which is sensitive to the ionization of the background gas near the laser focus in the target chamber.] Thus, electrons escape to the charge collectors with energy $\epsilon_e(t) = \epsilon_{br}(t) - e\phi_p(t)$, and this is plotted in the lower graph of Fig. 19. This temporal behavior of $\epsilon_e(t)$ results in the spectra shown in Fig. 20. $N(\epsilon)$ is essentially flat out to an energy ϵ_s determined by space charge, and then drops off in a remarkably straight "suprathermal tail". The slope of the tail, and hence T_h, is similar for all three curves.

The fractional laser absorption, f_{abs}, and hence the strength of the space-charge potential, was set rather arbitrarily in this calculation. It is important to ask how changes in f_{abs} affect the spectra in Fig. 20. If f_{abs} is increased, then fast electrons escape in greater numbers during the first few psec of breakdown. This faster buildup of space charge causes the breakpoint energy ϵ_s to increase and reduces the number of electrons emitted with energies below ϵ_s. Importantly, we find that varying f_{abs} between 0.05 and 1.0 has no effect on the slope of the tail and little effect on the total emitted charge, $\eta_t = \int_0^\infty N(\epsilon)d\epsilon$. In other words, T_h is not affected by space charge, although the total electron emission is space-charge limited. This model predicts $\eta_t \sim 6 - 12 \times 10^9$ under all conditions, and this is in quite good agreement with the experimental observation $\eta_t \sim 3 \times 10^9$. In a real experiment, because of variations in laser prepulse level or shock-tube discharge characteristics, the background gas ionization level, and thus f_{abs}, fluctuates from shot-to-shot. This explains our experimental observations that $n_h \equiv N_h k T_h \propto f_{abs}$ suffers order-of-magnitude fluctuations from shot-to-shot, while T_h and η_t are reproducible.

We regard these accurate predictions as a major success of our model.

The slopes of the suprathermal tails in the spectra of Fig. 20 were fitted by eye to a function $N(\epsilon) = N_h \exp(-\epsilon/kT_h)$. This yielded the dependences on E_p and p shown in Fig. 21. The calculated scaling, $T_h \propto E_p^{0.09} p^{0.16}$, is in extraordinary agreement with experimental observations. It must be admitted that the magnitude of T_h, typically 20 keV here, is 25% lower than observed in the laboratory, and that $n_h = N_h k T_h = 1 - 7 \times 10^{10}$ is about an order of magnitude too high. However, this may be just a reflection of the crude accounting of the electric field evanescence in the overdense plasma in this model. Also, T_h is clearly sensitive to the laser pulse shape, which is not known exactly. Finally, since $n_h \propto f_{abs}$, the value of n_h may simply indicate weaker absorption of laser light than was actually assumed.

The conclusion to be drawn from this calculation is that electron emission produced by a short-risetime laser pulse is dominated by a transient, "chirped" burst of instantaneously monoenergetic electrons. The observed spectrum is determined by the integrated temporal variation of the energy of that burst. This spectrum depends only weakly on experimental parameters. The simple model we propose explains our observations of space-charge-limited total emission, reproducible T_h, and fluctuating n_h, and accurately accounts for our observed scaling of T_h with pressure and laser pulse energy. This mechanism may have importance for laser fusion because it allows substantial numbers of electrons to be emitted before space-charge limitations set in, and because such emission may be active during the initial stages of breakdown of any laser target. By contrast, 500 psec FWHM laser pulses allow enough time for the establishment of a quasi-steady-state plasma density profile, determined by the ponderomotive force of the laser light. The observed spectrum behaves as predicted by that model.

ACKNOWLEDGMENTS

We are indebted to Al Franzosa for superb technical support in the construction of the apparatus. We also thank Jerry Black, for the care of our computer, and Tom Simpson, for help in installing our 10-atmosphere TE laser.

This work was supported by Department of Energy contract number DE-AC02-76DP40018.A001 (formerly ED-78-S-02-4631).

[1]J. P. Freidberg, R. W. Mitchell, R. L. Morse, and L. I. Rudsinski, Phys. Rev. Lett. **28**, 795 (1972).
[2]J. Albritton and P. Koch, Phys. Fluids **18**, 1136 (1975).
[3]K. Eidman and R. Sigel, Phys. Rev. Lett. **34**, 799 (1975).
[4]K. R. Manes, V. C. Rupert, J. M. Auerbach, P. H. Y. Lee, and J. E. Swain, Phys. Rev. Lett. **39**, 281 (1977); J. S. Pearlman and M. K. Matzen, Phys. Rev. Lett. **39**, 140 (1977); J. S. Pearlman, J. J. Thomson, and C. E. Max, Phys. Rev. Lett. **38**, 1397 (1977).
[5]J. F. Kephart, R. P. Godwin, and G. H. McCall, Appl. Phys. Lett. **25**, 108 (1974).
[6]R. L. Stenzel, A. Y. Wong, and H. C. Kim, Phys. Rev. Lett. **32**, 654 (1974).
[7]P. Kolodner and E. Yablonovitch, Phys. Rev. Lett. **37**, 1754 (1976).
[8]Yu. P. Raizer, Zh. Eksp. Teor. Fiz. **48**, 1508 (1965) [Sov. Phys.-JETP **21**, 1009 (1965)].
[9]V. L. Ginzburg, *Propagation of Electromagnetic Waves in Plasmas* (Pergamon, New York, 1964).
[10]K. G. Estabrook, E. Valeo, and W. L. Kruer, Phys. Lett. **49A**, 109 (1974).
[11]D. W. Forslund, J. M. Kindel, and K. Lee, Phys. Rev. Lett. **39**, 284 (1977); K. G. Estabrook and W. L. Kruer, Phys. Rev. Lett. **40**, 42 (1978).
[12]B. Bezzerides, S. J. Gitomer, and D. W. Forslund, Phys. Rev. Lett. **44**, 651 (1980).
[13]J. S. deGroot and J. E. Tull, Phys. Fluids 18, 672 (1975).
[14]J. N. Bradley, *Shock Waves in Chemistry and Physics* (Methuen, London, 1962).
[15]R. A. Gross, Rev. Mod. Phys. **37**, 724 (1965).
[16]H. Ahlsmeyer, J. Fluid Mech. **74**, 497 (1976).
[17]C. A. Boitnott and R. C. Warder, Phys. Fluids **14**, 2312 (1971). G. Lensch and H. Gronig, in *Proceedings of the 11th International Symposium on Shock Tubes and Waves* (University of Washington Press, Seattle, 1978), p. 132.
[18]J. H. Kieffer and R. W. Lutz, J. Chem. Phys. **44**, 658 (1966); M. J. Yoder, *ibid.* **56**, 3226 (1972).
[19]E. Yablonovitch, Phys. Rev. A **10**, 1888 (1974).
[20]H.-S. Kwok and E. Yablonovitch, Opt. Commun. **21**, 252 (1977).
[21]H.-S. Kwok and E. Yablonovitch, Rev. Sci. Instrum. **46**, 814 (1975).
[22]H.-S. Kwok and E. Yablonovitch, Appl. Phys. Lett. **30**, 158 (1977).
[23]J. G. Black, P. Kolodner, M. J. Schultz, E. Yablonovitch, and N. Bloembergen, Phys. Rev. A **19**, 704 (1979).
[24]H. Brinkschulte, Z. Naturforsch. **22a**, 438 (1967).
[25]G. J. Pert, J. Appl. Phys. **39**, 5932 (1968).
[26]L. Pages, E. Bertel, H. Joffre, and L. Sklavenitis, Atomic Data **4**, 1 (1972).
[27]R. A. Cairns, Plasma Phys. **20**, 991 (1978).
[28]E. Yablonovitch, Appl. Phys. Lett. **23**, 121 (1973).
[29]E. Yablonovitch, Phys. Rev. Lett. **35**, 1346 (1975).
[30]H.-S. Kwok, Ph.D. thesis, Harvard University, 1978.